



Research Article

Annealed microstructure dependent corrosion behavior of Ti-6Al-3Nb-2Zr-1Mo alloy

Baoxian Su^a, Liangshun Luo^{a,*}, Binbin Wang^a, Yanqing Su^{a,*}, Liang Wang^a, Robert O. Ritchie^b, Enyu Guo^c, Ting Li^d, Huimin Yang^e, Haiguang Huang^{f,g}, Jingjie Guo^a, Hengzhi Fu^a

^a National Key Laboratory for Precision Hot Processing of Metals, School of Materials Science and Engineering, Harbin Institute of Technology, Harbin 150001, China

^b Department of Materials Science and Engineering, University of California, Berkeley, CA 94720, USA

^c Key Laboratory of Solidification Control and Digital Preparation Technology (Liaoning Province), School of Materials Science & Engineering, Dalian University of Technology, Dalian, 116024, China

^d Department of Materials Science and Engineering, Dalian Maritime University, Dalian 116026, China

^e School of Materials and Chemical Engineering, Heilongjiang Institute of Technology, Harbin 150050, China

^f School of Materials Science and Engineering, Kunming University of Science and Technology, Kunming 650093, China

^g Yunnan Titanium Industry Co., Ltd., Chuxiong 651209, China

ARTICLE INFO

Article history:

Received 9 April 2020

Received in revised form 23 May 2020

Accepted 24 May 2020

Available online 9 July 2020

Keywords:

Titanium alloys

Annealing

Electrochemical techniques

Weight loss

Corrosion behavior

ABSTRACT

Corrosion resistance of titanium (Ti) alloys is closely connected with their microstructure which can be adjusted and controlled via different annealing schemes. Herein, we systematically investigate the specific effects of annealing on the corrosion performance of Ti-6Al-3Nb-2Zr-1Mo (Ti80) alloy in 3.5 wt.% NaCl and 5 M HCl solutions, respectively, based on open circuit potential (OCP), potentiodynamic polarization, electrochemical impedance spectroscopy (EIS), static immersion tests and surface analysis. Results indicate that increasing annealing temperature endows Ti80 alloy with a higher volume fraction of β phase and finer α phase, which in turn improves its corrosion resistance. Surface characterization demonstrates that β phase is more resistant to corrosion than α phase owing to a higher content of Nb, Mo, and Zr in the former; additionally, the decreased thickness of α phase alleviates segregation of elements to further restrain the micro-galvanic couple effects between α and β phases. Meanwhile, the influential mechanisms of environmental conditions on corrosion of Ti80 alloy are discussed in detail. As the formation of a highly compact and stable oxide film on surface, annealed Ti80 alloys exhibit a low corrosion current density (10^{-6} A/cm²) and high polarization impedance (10^6 $\Omega \cdot \text{cm}^2$) in 3.5 wt.% NaCl solution. However, they suffer severe corrosion in 5 M HCl solution, resulting from the breakdown of native oxide films (the conversion of TiO₂ to aqueous Ti³⁺), active dissolution of substrate Ti to aqueous Ti³⁺ and existence of micro-galvanic couple effects. Those findings could provide new insights to designing Ti alloys with high-corrosion resistance through microstructural optimization.

© 2020 Published by Elsevier Ltd on behalf of The editorial office of Journal of Materials Science & Technology.

1. Introduction

Given their excellent corrosion resistance, titanium (Ti) alloys are increasingly used for applications in chemical industry, desalination of seawater, offshore drilling, marine, and biomaterials [1–5]. Previous reports have showed that the corrosion performance of Ti alloys is closely related to their microstructure which

can be tailored by their alloy chemical composition [6,7], and/or external processes [3,8–12]. For instance, heat treatment provides an expedient and practical means to adjust and control the microstructure to further meet the desired corrosion resistance and even mechanical properties of Ti alloys [13,14].

In this regard, Geetha et al. [15] evaluated the effects of solution treatment on the corrosion performance of Ti-13Nb-13Zr alloy in Ringer's solution and reported that the water-quenched $\alpha + \beta$ microstructure exhibits superior corrosion resistance owing to the uniform distribution of alloying elements in different phases. In a similar vein, Atapour et al. [16] evaluated the corrosion behav-

* Corresponding authors.

E-mail addresses: llshun@163.com (L. Luo), suyq@hit.edu.cn (Y. Su).

ior of Ti-6Al-4 V alloy fabricated by different heat treatments and reported that volume fractions of primary α and transformed β can play a significant role in affecting the corrosion resistance. To further elucidate this effect, Yang et al. [13], in a study of influence of annealing temperature on the corrosion behavior of Ti-20Zr-6.5Al-4 V alloy, found that the thickness of α phase and volume fraction of retained β phase which are closely related to annealing temperature, are two primary determinant factors for the corrosion resistance. This was verified by Longhitano et al. [17] in their investigation of additively manufactured Ti-6Al-4 V ELI alloy, where the nucleation and growth of β phase during heat treatment are observed to strongly affect the corrosion resistance. Accordingly, it is essential to find an optimum heat treatment and establish a relationship between annealed microstructure and corrosion behavior for the design and development of high-corrosion resistance Ti alloys. In the current work, we would systematically study the influences of different annealing temperatures on the microstructure and corrosion resistance of Ti-6Al-3Nb-2Zr-1Mo (a new near- α Ti alloy, abbreviated as Ti80), which has not been reported yet.

In addition to annealing-induced microstructural changes, the nature of environment can also significantly affect the corrosion behavior of Ti alloys [15]. Various studies have reported that Ti alloys exhibit excellent corrosion resistance in natural waters and brine solutions due to the existence of native oxide films mainly composed of TiO_2 [2,10,18]. Furthermore, they are generally resistant to corrosion in strongly oxidizing environments such as chromic acid, perchloric acid, and nitric acid that can promote the formation of a stable TiO_2 oxide film [19]. However, Ti alloys exhibit relatively poor corrosion resistance in reducing acids such as sulfuric acid and hydrochloric acid, where the protective native oxide films can be destroyed [19]. Therefore, it is essential to adopt appropriate and effective strategies to improve the corrosion performance of Ti alloys in reducing acid environments. To this end, a typical strong reducing acid solution, *i.e.*, 5 M HCl solution [13,18,20], was selected to evaluate the specific effects of different annealing temperatures on the corrosion performance of Ti80 alloys in reducing acid environments. Additionally, to simulate the role of seawater or other system containing Cl^- ions, 3.5 wt.% NaCl solution was used, similar to previous studies [2,9,10].

In this study, by systematically analyzing the results of electrochemical and static immersion measurements of annealed Ti80 alloys in 3.5 wt.% NaCl and 5 M HCl solutions, we demonstrate a strong effect of different annealing temperatures, and hence specific microstructure, on the corrosion behavior of Ti80 alloy. Additionally, based in part on surface analysis, the salient mechanisms corrosion in this alloy are discussed.

2. Materials and methods

2.1. Materials

Ti80 alloy was prepared by melting a mixture of pure elements of Ti, Al, Nb, Zr and Mo (with purity above 99 wt.%) in a consumable electrode vacuum arc furnace. The resulting ingot was remelted at least three times to ensure compositional homogeneity. Phase transformation temperatures of Ti80 alloy were determined using differential scanning calorimetry (DSC, STA449F3, Netzsch, Germany). DSC tests were performed by heating about 100 mg of material to 1150 °C in a high-purity argon atmosphere with a heating rate of 20 °C/min. As shown in Fig. 1a, the nominal $\alpha \rightarrow \alpha + \beta$ and $\alpha + \beta \rightarrow \beta$ transformation temperatures for Ti80 alloy were approximately 831 and 1011 °C, respectively.

Based on the measured phase transition temperatures, multiple thermomechanical excursions were performed, as shown in Fig. 1b. The first two forgings at 1150 and 1020 °C were performed

within β phase region to break the coarse cast structure, whereas the last three forgings were carried out at 950 °C within $\alpha + \beta$ phase region. Specimens with a dimension of 100 × 15 × 15 mm³ were fabricated using electrical discharge machining from the resulting multiply forged material for subsequent annealing treatments. In this study, four different annealing temperatures, $T = 850, 900, 950,$ and 1000 °C, were selected. Annealing treatments were conducted in a tubular vacuum furnace under a protective argon atmosphere to prevent oxidation. Specimens were held at the selected annealing temperature for 2 h, and then followed by air cooling (AC) to room temperature.

2.2. Microstructure characterization

X-ray diffraction (XRD) was performed, using a unit made by Epyrean, PANALytical, Netherlands, with Bragg-Brentano geometry and Cu K α radiation, to analyze phase compositions. Microstructure characterization was respectively carried out using an Olympus-GX71 microscope (Olympus Corporation, Japan), a JXA-8230 microscope (JEOL, Japan) and a Talos F200X microscope (FEI, USA). Specimens for optical microscopy (OM) and scanning electron microscopy (SEM) analysis, with a dimension of 10 × 10 × 5 mm³, were first ground with SiC papers to 2000 grit, then polished with 1 μm diamond paste, and finally etched in Kröll's reagent, *i.e.*, 10 vol.% HF, 10 vol.% HNO_3 , 80 vol.% H_2O . Prior to characterization, all specimens were cleaned with acetone and alcohol. Corresponding transmission electron microscopy (TEM) specimens were prepared by electrolytic thinning in a solution containing 90 mL of methanol and 10 mL of perchloric acid at approximately –35 °C.

2.3. Electrochemical measurements

Electrochemical experiments were carried out for annealed Ti80 alloys at a temperature of 25 ± 1 °C maintained by a thermostatic water bath. For electrochemical measurements, a typical three-electrode electrochemical cell system was used, with a saturated calomel electrode (SCE) as reference electrode, a platinum plate as counter electrode and test specimen used as working electrode. Specimens for such electrochemical testing, with a dimension of 10 × 10 × 5 mm³, were first ground using 400 grit SiC papers; then an insulated copper wire was connected to the back of specimens using conducting resin to avoid undesirable ohmic effects; finally, all specimens were embedded in epoxy resin, leaving an exposed surface area of 1 cm².

Before each electrochemical test, open circuit potential (OCP) was recorded for 9000 s, which was long enough for the OCP to become stable. Potentiodynamic polarization curves were recorded from –1000 mV to 2000 mV vs. SCE after OCP tests. A very slow potential sweep rate of 0.1667 mV/s was used to ensure a near steady-state condition. Electrochemical impedance spectroscopy (EIS) experiments were performed at OCP immediately after 2.5 h immersion with a sinusoidal potential perturbation of 10 mV rms (root mean square) in a scan frequency ranging from 10^{–2} Hz to 10⁵ Hz. Dozen points per decade were recorded during EIS measurements. The EIS data were fitted and analyzed using ZSimpWin 3.10 software. For each condition, at least three specimens were tested to ensure reproducibility.

2.4. Static immersion test

Static immersion tests were carried out in accordance with ASTM Standard G31–72 [21]. Based on previous studies [13,18], considerable variations in weight loss and corroded morphologies can be observed for Ti alloys tested in strongly reducing HCl solutions due to their relatively poor corrosion resistance; this is in

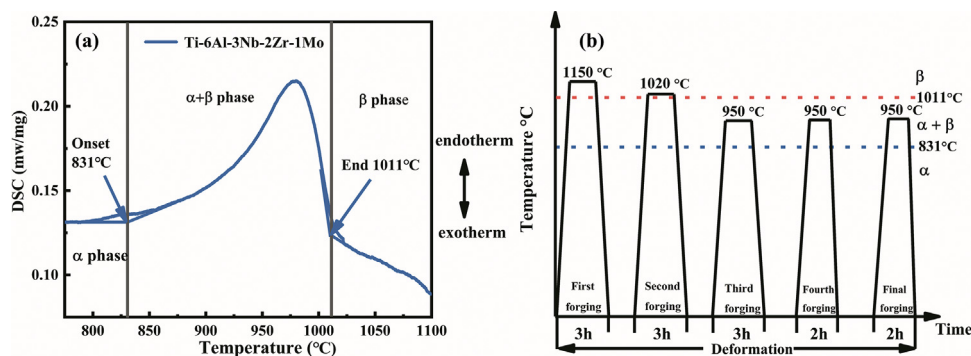


Fig. 1. (a) DSC curve and (b) a schematic diagram showing the processing route utilized for Ti80 alloy.

contrast to the mere slight differences observed in near neutral pH NaCl solutions at 25 °C. Therefore, to gain insight into the structural metrics of annealing-dependent corrosion behavior of Ti80 alloy, we selected a common 5 M HCl solution as the static immersion tests solution. The temperature of this solution was maintained at 25 ± 1 °C throughout the entire immersion period. Specimens for static immersion tests, which were also $10 \times 10 \times 5$ mm³ in size, were ground using 240 grit SiC papers, ultrasonically cleaned with acetone, alcohol, and distilled water successively for 5 min, dried with cold air, and then carefully weighed using an analytical balance (ME204E, Mettler Toledo Corp., Switzerland) with an accuracy of ± 0.1 mg. The exposed area of each specimen was calculated independently by the geometry dimension prior to being immersed in a container with 100 mL naturally aerated 5 M HCl solution. Specimens were taken out every two days over a period of 10 days, cleaned with acetone, alcohol, and distilled water sequentially to remove corrosion products, dried and weighed before being placed in freshly prepared solution for next 2 days. The immersed specimens were reused for each immersion interval. For each test, three specimens were tested to ensure reproducibility; average values are reported.

SEM was used to observe surface morphologies of corroded specimens after static immersion tests. In addition, another group of specimens were immersed in 5 M HCl solution for only 4 h and then observed using an atomic force microscopy (AFM, Dimension Fastscan, Bruker, USA) to further examine the specifics of corrosion process.

2.5. X-ray photoelectron spectroscopy (XPS) analysis

XPS tests were performed on an ESCALAB 250Xi unit (Thermo Fisher, USA) to analyze the chemical composition of surface corrosion product films. X-ray photoelectron spectrometer was equipped with Al-K α radiation at 1486.6 eV, with a working potential of 12.5 kV, a filament current of 16 mA, and a X-ray spot size of 500 μ m. Survey spectra were recorded with a pass energy of 100 eV at an energy step size of 1 eV, and high-resolution spectra were taken with a pass energy of 20 eV at an energy step size of 0.05 eV. In addition, the binding energy was calibrated using C 1s peak (284.6 eV) from carbon contamination. The XPS spectra of different elements were analyzed using CasaXPS software.

3. Results

3.1. Microstructure characterization

Fig. 2a displays XRD patterns of annealed Ti80 alloys. Standard peak positions of α -Ti (JCPDS 00–44–1294) and β -Ti (JCPDS 00–44–

1288) are also presented in Fig. 2a to identify the phase constitution. All annealed Ti80 alloys are consisted of α phase with hexagonal close-packed (*hcp*) structure and β phase with body-centered cubic (*bcc*) structure. However, β phase (1 1 0) reflection peak (near $2\theta = 38.5^\circ$) changes with annealing temperature; specifically, β (110) reflection peak gradually broadens and the intensity increases with increasing annealing temperature. To further evaluate annealing-induced changes of β phase, volume fraction of β phase is calculated through XRD fitting. Variations in volume fraction of β phase vs. annealing temperature are plotted in Fig. 2b. Volume fraction of β phase increases from 4.7 % to 5.7 % with annealing temperature increasing from 850 to 1000 °C, i.e., the precipitations of β phase in those Ti alloys can be promoted by increasing annealing temperature.

Fig. 3a–h exhibits microstructure of annealed Ti80 alloys. As depicted in Fig. 3a, e, the specimen annealed at 850 °C is mainly composed of primary equiaxed α phase and retained β phase. The presence of a large number of primary equiaxed α phases should be attributed to the incomplete phase transition from primary α phase to β phase during annealing, resulting from a low annealing temperature and short holding time. As annealing temperature increases to 900 °C, volume fraction of primary α phase decreases, but share of secondary lamellar α phase correspondingly increases, leading to a reduction in the mean thickness of α phase, as mapped in Fig. 3b, f. When the specimen anneals at 950 °C, the microstructure presents a typical Widmanstätten structure (Fig. 3c). Prior β grain boundaries can be clearly observed, and the substructure exhibits a basket-weave arrangement of slender α laths. After annealing at 1000 °C, the specimen shows a fully lamellar microstructure as this annealing temperature is very close to the β -transus temperature of 1011 °C. Moreover, some extremely fine β phases distributes among lamellar α phases (Fig. 3h), to be the well-known $\alpha/\beta/\alpha$ sandwich microstructure, consistent with the results reported in ref. [3]. In addition, the average thickness of α phase, d , is evaluated to determine how it varies with annealing temperature; the measured data can be found in Fig. 3i. Notably, the mean thickness of α phase d significantly decreases from 9.18 μ m to 0.59 μ m as annealing temperature increases from 850 to 1000 °C.

Fig. 3j depicts a typical high-angle angular dark field (HAADF) image and scanning transmission electron microscopy (STEM) elemental maps of Ti80 alloy after annealing at 1000 °C. The α and β phases can be clearly identified from the HAADF image. In addition, STEM elemental maps reveal that Al is abundant in α phase, while Mo and Nb are enriched in β phase. Although Zr is generally considered to be a neutral element, it is more inclined to be distributed in β phase in this study. Relative concentrations of alloying elements in α and β phases of annealed Ti80 alloys are listed in Table 1.

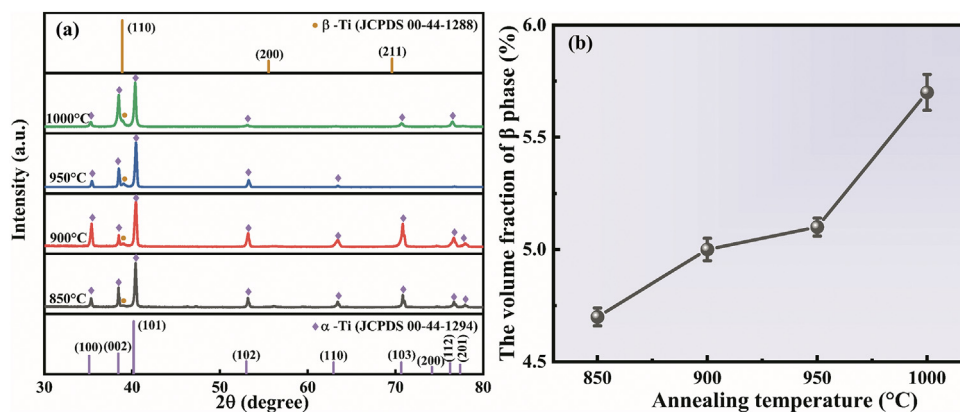


Fig. 2. XRD results of Ti80 alloy annealed at temperatures between 850 and 1000 °C: (a) XRD patterns, (b) volume fraction of β phase, vs. annealing temperature.

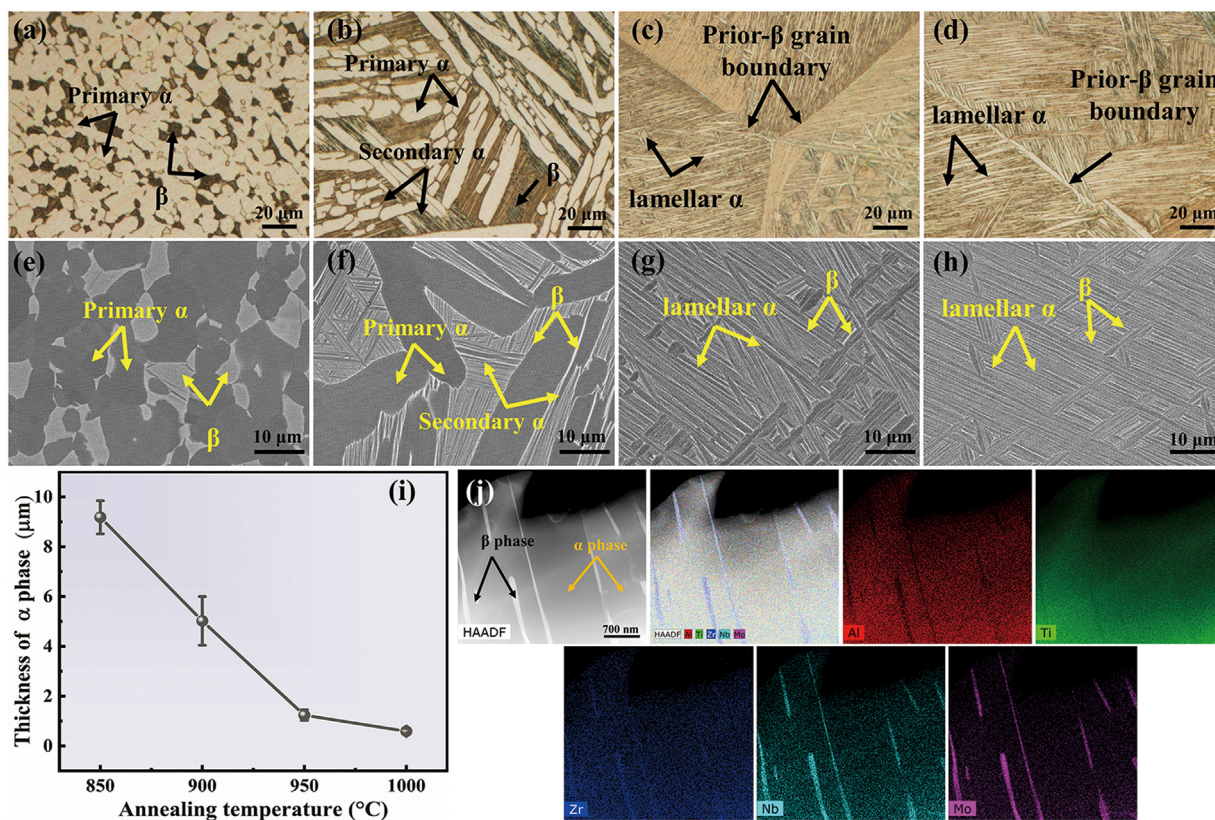


Fig. 3. Microstructure in Ti80 alloy annealed at different temperatures, as shown by OM (a to d) and SEM (e to h) images. Microstructure after annealing at (a) and (e) 850 °C, (b) and (f) 900 °C, (c) and (g) 950 °C, and (d) and (h) 1000 °C. (i) The mean thickness d of α phase, i.e., the average value of intersecting diagonals (ASTM E112-12), varies with annealing temperature. (j) Typical HAADF image and STEM elemental maps of Ti80 alloy annealed at 1000 °C.

Table 1
Concentration of alloying elements in α and β phases of annealed Ti80 alloys.

Specimen	Relative concentration (wt.%)					
	Phase	Ti	Al	Nb	Zr	Mo
850 °C	α (hcp)	Balance	6.78 ± 0.19	2.75 ± 0.20	2.32 ± 0.11	0.84 ± 0.22
	β (bcc)	Balance	4.31 ± 0.08	7.35 ± 0.21	2.85 ± 0.36	4.76 ± 0.36
900 °C	α (hcp)	Balance	6.68 ± 0.16	3.04 ± 0.07	2.08 ± 0.04	1.05 ± 0.12
	β (bcc)	Balance	5.00 ± 0.12	6.34 ± 0.22	2.42 ± 0.09	3.48 ± 0.32
950 °C	α (hcp)	Balance	6.46 ± 0.09	2.78 ± 0.03	1.90 ± 0.07	1.31 ± 0.12
	β (bcc)	Balance	5.55 ± 0.08	3.96 ± 0.28	2.17 ± 0.03	2.23 ± 0.26
1000 °C	α (hcp)	Balance	6.24 ± 0.02	2.97 ± 0.05	1.96 ± 0.05	1.27 ± 0.06
	β (bcc)	Balance	5.85 ± 0.06	3.57 ± 0.13	2.11 ± 0.02	1.48 ± 0.06

3.2. Corrosion behavior

3.2.1. OCP measurements

Fig. 4 displays the OCP response of annealed Ti80 alloys immersed in different solutions for 9000 s. In 3.5 wt.% NaCl solution (Fig. 4a), the OCP of each specimen gradually shifts to a nobler potential and finally reaches a relatively higher potential, corresponding to the growth of protective oxide film on electrode surface [22]. In addition, some fluctuations of OCP curves are observed, mainly resulting from the simultaneous competition between film formation and dissolution [2]. However, different scenarios can be noticed in 5 M HCl solution (Fig. 4b); the OCP first slowly decreases with time and then dramatically reduces to a relatively lower potential, attributed to the chemical dissolution of native oxide films [19]. Fig. 4b also reveals that the activation time of annealed Ti80 alloys can be prolonged with increasing annealing temperature, indicating a much more stable native oxide film [23]. In addition, Fig. 4a, b respectively illustrates that increased annealing temperature can promote the terminal value of OCP in 3.5 wt.% NaCl and 5 M HCl solutions. It means higher annealing temperature can enhance the thermodynamic ability of Ti80 alloy to resist corrosion [24], which is derived from the variations in the thickness of α phase and volume fraction of β phase induced by different annealing temperatures.

3.2.2. Potentiodynamic polarization test

Potentiodynamic polarization curves of annealed Ti80 alloys can be obtained after OCP tests; results are presented in Fig. 5a, b. In 3.5 wt.% NaCl solution (Fig. 5a), there is no obvious difference between those cathodic polarization curves, indicating the occurrence of a similar cathodic reaction [25]. For anodic branches, each annealed alloy directly enters a large and steady passivation region, where the current density remains unchanged despite the increase in potential. The passive film formed in this region on electrode surface prevents annealed Ti80 alloys from dissolution. In Fig. 5b, all annealed Ti80 alloys also exhibit a similar cathodic reaction in 5 M HCl solution, mainly corresponding to the hydrogen evolution reaction (HER). In anodic branches, there are three typical types of behavior.

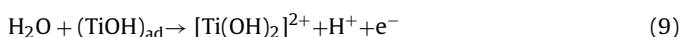
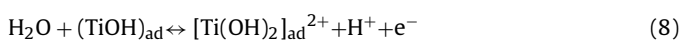
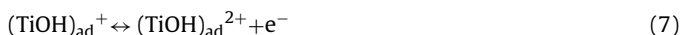
(I) *Active dissolution region.* In this region, substrate Ti is oxidized to form soluble Ti^{3+} ions through the following reactions [26]:



Then, $(\text{TiOH})_{\text{ad}}^{2+}$ is dissolved to soluble Ti^{3+} species in 5 M HCl solution, as described by the following reaction:



(II) *Active-passive transition region.* The maximum anodic current is indicative of the beginning of active-passive transition region. In this region, although reactions (1) - (6) are still popular, other additional dominant reactions can also occur which limit current flow through interface [26]:



The declining current in active-passive transition region should be attributed to the formation of anodically-grown passivating oxide films, as in reaction (11).

(III) *Passive region.* Following the active-passive transition, anodic branches enter the passive region, approximately from -250 mV to 1.25 V. In this region, the surface of annealed Ti80 alloys covers with anodically-grown passivating oxide films. Some current fluctuations are also observed, resulting from the simultaneous competition between the formation and dissolution of anodically-grown passivating oxide films, as in reversible reaction (11). In addition, a common transition current can be observed at -1.5 V vs. SCE in both Fig. 5a, b, which should be attributed to the oxidation behavior of solution [27,28].

Corrosion current density (i_{corr}) is generally used to evaluate the corrosion resistance. For the spontaneous passive behavior of annealed Ti80 alloys in 3.5 wt.% NaCl (Fig. 5a), i_{corr} can be approximately regarded as equal to i_{pass} [22,30], which is obtained at 500 mV. However, for an active system, e.g., 5 M HCl solution (Fig. 5b), i_{corr} is determined by extrapolating cathodic Tafel lines to the corrosion potential (E_{corr}); this is adopted because no well-defined experimental anodic Tafel regions are present in polarization curves [29,30]. The obtained values of i_{corr} and E_{corr} are listed in Table 2. For more intuitive observation, variations in i_{corr} and E_{corr} with annealing temperature are plotted in Fig. 6a, 6b, respectively. As seen in Fig. 6a, it is evident that i_{corr} decreases with the increase in annealing temperature in both NaCl and HCl solutions. In Fig. 6b, as annealing temperature raises, E_{corr} increases, i.e., polarization curves shift towards a more positive potential. Indeed, the decreased i_{corr} and increased E_{corr} provide a definite indicator of an enhanced corrosion resistance with increasing annealing temperature, in terms of both corrosion kinetics and thermodynamics. The corrosion rate I can be calculated using the following equation [31]:

$$I(\text{mm} \cdot \text{year}^{-1}) = 3.28 \times i_{\text{corr}} \times (M/n\rho) \quad (12)$$

where M is the atomic weight of Ti (47.87 g), n is the number of electrons transferred in the corrosion reaction ($n = 3$, corresponding to the conversion of Ti to Ti^{3+}), and ρ is the density of Ti ($4.51 \text{ g} \cdot \text{cm}^{-3}$). The calculated values of I in 5 M HCl solution are listed in Table 2. As annealing temperature increases from 850 to 1000 °C, corrosion rate decreases from $1.89 \text{ mm} \cdot \text{year}^{-1}$ to $1.37 \text{ mm} \cdot \text{year}^{-1}$ in 5 M HCl solution, reinforcing our conclusion that raising annealing temperature can provide a beneficial enhancement in corrosion resistance of those titanium alloys.

3.2.3. Electrochemical impedance spectroscopy (EIS) measurements

To further elucidate the special effects of different annealing temperatures on the corrosion performance of Ti80 alloy, impedance spectra were measured in 3.5 wt.% NaCl and 5 M HCl solutions, respectively. The corresponding Nyquist plots and Bode plots are presented in Fig. 7.

Fig. 7a displays the Nyquist plots of annealed Ti80 alloys after 2.5 h immersion in 3.5 wt.% NaCl solution. All Nyquist plots exhibit a single capacitive loop, generally corresponding to one capacitive time constant. This is caused by the formation of a highly stable and compact oxide film on surface [22,32]. Here, the diameter of capacitive loop represents the resistance; in general, a larger diameter indicates a higher resistance [33]. The inference from Fig. 7a is again that an increase in annealing temperature can enhance the corrosion resistance of annealed Ti80 alloys in 3.5 wt.% NaCl solution. However, in 5 M HCl solution (Fig. 7c), all Nyquist plots show two obvious capacitive loops, i.e., two well-separated semi-circles, which indicates the existence of two capacitive time constants [34,35]. The high frequency capacitive loop could be attributed to the electric double layer at the interface between electrolyte solu-

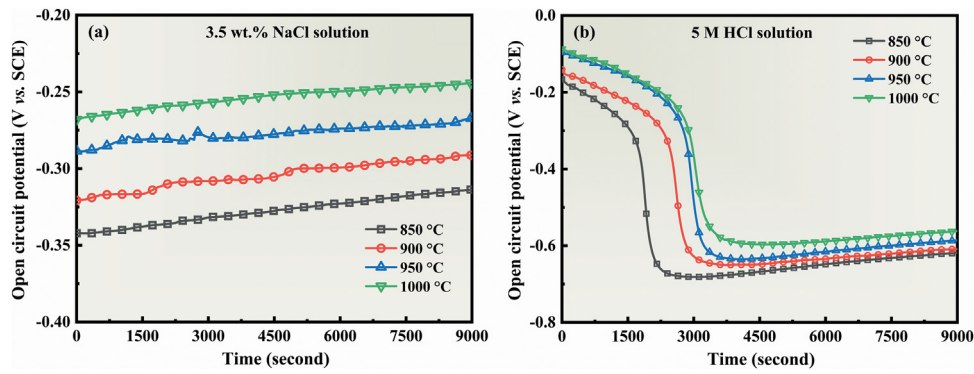


Fig. 4. Variations of open circuit potential (OCP) with time for annealed Ti80 alloys in (a) 3.5 wt.% NaCl solution and (b) 5 M HCl solution.

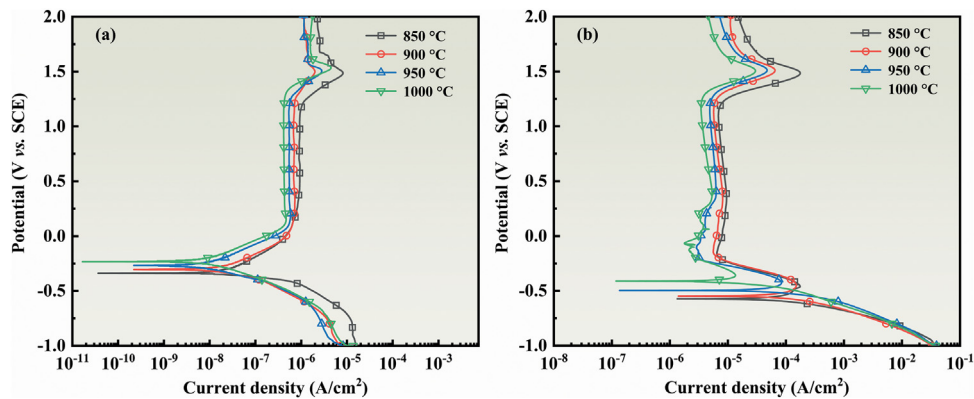


Fig. 5. Potentiodynamic polarization curves of annealed Ti80 alloys in (a) 3.5 wt.% NaCl solution and (b) 5 M HCl solution.

Table 2

Parameters deduced from potentiodynamic polarization curves.

Annealing temperature (°C)	In 3.5 wt.% NaCl solution		In 5 M HCl solution			Corrosion rate (mm·year ⁻¹)	
	E_{corr} (V vs. SCE)	i_{corr} (μA cm ⁻²)	E_{corr} (V vs. SCE)	i_{corr} (μA cm ⁻²)	β_c (mV·decade ⁻¹)	Obtained from i_{corr}	Obtained from weight loss
850	-0.345 ± 0.011	0.937 ± 0.028	-0.605 ± 0.013	162.51 ± 2.86	-131 ± 7	1.89 ± 0.04	1.91 ± 0.21
900	-0.303 ± 0.009	0.728 ± 0.022	-0.574 ± 0.005	146.13 ± 2.05	-153 ± 5	1.70 ± 0.02	1.64 ± 0.05
950	-0.265 ± 0.015	0.591 ± 0.014	-0.545 ± 0.008	131.07 ± 1.13	-152 ± 4	1.52 ± 0.02	1.54 ± 0.01
1000	-0.223 ± 0.018	0.461 ± 0.031	-0.484 ± 0.016	118.32 ± 0.85	-154 ± 2	1.37 ± 0.01	1.42 ± 0.02

tion and Ti80 alloy substrate, whereas the low frequency capacitive loop could be assigned to the corrosion product film on alloy. Moreover, the diameters of both high-frequency and low-frequency capacitive loops are enhanced, indicating that both charge transfer resistance and corrosion product film resistance can be improved by increasing annealing temperature.

Regarding Bode plots in 3.5 wt.% NaCl (Fig. 7b), only one peak is observed in all Bode-phase plots, i.e., Bode-phase plots also suggests one time constant [36]. Bode-phase curves show that phase angles of all annealed Ti80 alloys are close to 90° over a wide frequency range, indicating the existence of a highly stable film on surface of all annealed Ti80 alloys in 3.5 wt.% NaCl solution [37,38]. Furthermore, the Impedance values obtained at the terminate frequency (10⁻² Hz) can reach 10⁶ Ω cm², which should be ascribed to the formation of a highly stable film. Fig. 7d displays Bode plots measured in 5 M HCl solution. Bode-phase plots contain two peaks, and two steps are observed on Bode-magnitude plots, all suggesting the appearance of two time constants [35,39]. Moreover, the Impedance at low frequency increases with annealing temperature, demonstrating that the corrosion resistance can be improved by increasing annealing temperature.

To further interpret the corrosion behavior of annealed Ti80 alloys, two typical equivalent circuits [9,10,40,41], presented in Fig. 8a, b, are proposed to fit the EIS data. In these two equivalent circuits, R_s is the solution resistance, CPE_{dl} and R_{ct} are respectively the constant phase element related to the electrical double layer capacitance and charge transfer resistance, and CPE_f and R_f are respectively the constant phase element associated with the oxide/corrosion product film capacitance and oxide/corrosion product film resistance. The CPE substitution of pure capacitance is used here through considering the time constant dispersion which originates from surface heterogeneities [35]. The impedance of CPE can be defined as follows [42,43]:

$$Z_{CPE} = [Q(j\omega)^n]^{-1} \tag{13}$$

where Q is the magnitude of CPE, j is an imaginary number ($j = \sqrt{-1}$), ω is angular frequency ($\omega = 2\pi f$, f is the frequency), n is the CPE exponent ranging from -1 to 1.

The EIS spectra measured in 3.5 wt.% NaCl solution can be well fitted using an equivalent circuit with one time constant (Fig. 8a), while the EIS spectra obtained in 5 M HCl solution can be fitted to an equivalent circuit with two time constants

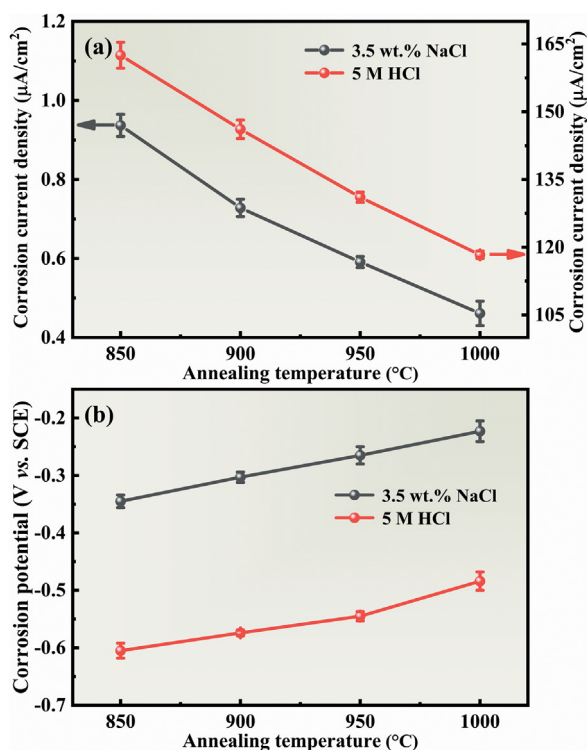


Fig. 6. The electrochemical parameters of annealed Ti80 alloys vary with annealing temperature: (a) corrosion current density and (b) corrosion potential.

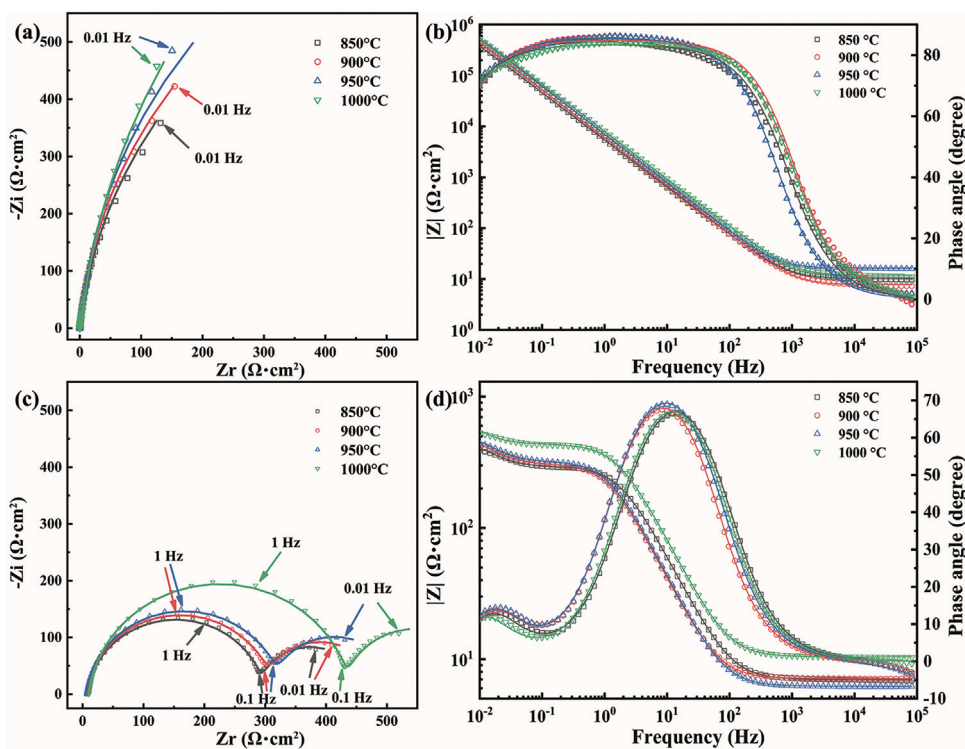


Fig. 7. Nyquist plots of annealed Ti80 alloys after 2.5 h immersion in (a) 3.5 wt.% NaCl solution, and (c) 5 M HCl solution. The corresponding Bode plots after 2.5 h immersion in (b) 3.5 wt.% NaCl solution, and (d) 5 M HCl solution. The solid curves are simulated results obtained by ZSimpWin.

(Fig. 8b). Nyquist plots (Fig. 7a, c) demonstrate that the experimental data are consistent with those obtained using complex non-linear least squares (CNLS) simulations for most frequencies, indicating the selected equivalent circuits are suitable. The detailed EIS fitting data for 3.5 wt.% NaCl and 5 M HCl solu-

tions are shown in Tables 3 and 4, respectively. The chi-square (χ^2) value is in the order of 10^{-3} to 10^{-4} , and the magnitude of sums of squares (λ^2) obtained for each annealed Ti80 alloy is reasonably close to zero, also revealing an excellent fitting quality [44]. The fitting error of each element is also listed in Table 3.

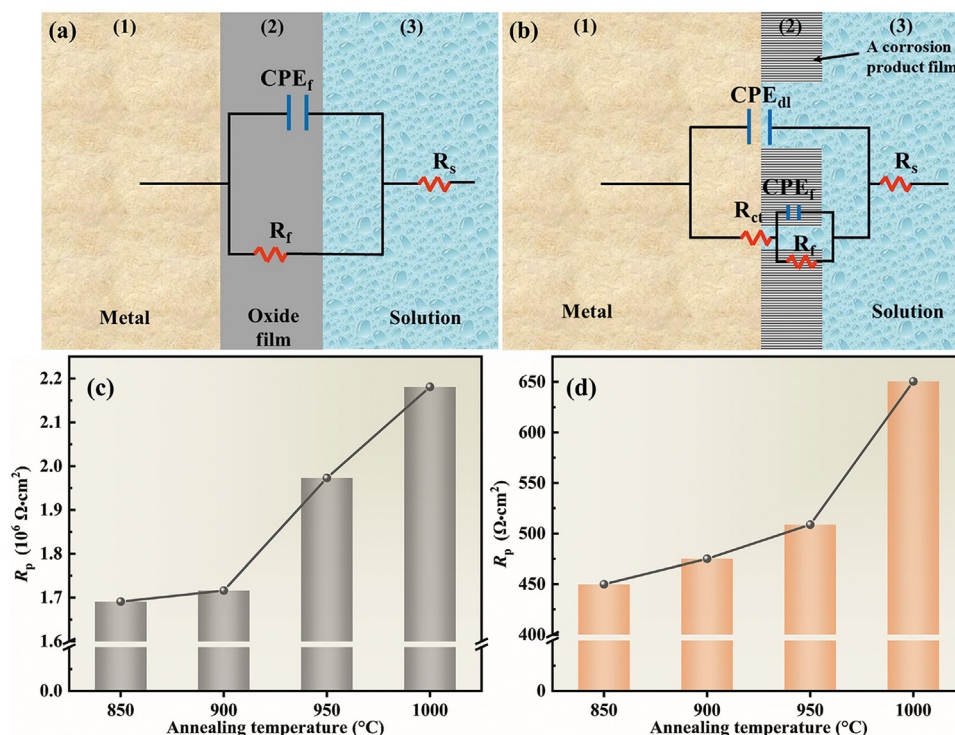


Fig. 8. The equivalent circuits used to fit the measured impedance data. (a) Equivalent circuit with one time constant, (b) equivalent circuit with two time constants. Variations of polarization resistance as a function of annealing temperature, in (c) 3.5 wt.% NaCl solution, and (d) 5 M HCl solution.

Table 3

Equivalent circuit parameters for annealed Ti80 alloys after 2.5 h immersion in 3.5 wt.% NaCl solution: R_s solution resistance, CPE_f constant phase element, n_f the exponent of CPE_f , R_f oxide film resistance. The Chi-square parameter (χ^2) and sums of squares (λ^2) obtained for each annealed Ti80 alloy. Besides, the calculated oxide film capacitance C_f and oxide film thickness d are listed.

Annealing Temperature (°C)	R_s ($\Omega \text{ cm}^2$)	CPE_f ($\mu\text{S}\cdot\text{s}^n \text{ cm}^{-2}$)	n_f	R_f ($10^6 \Omega \text{ cm}^2$)	χ^2 (10^{-3})	λ^2	C_f ($\mu\text{F cm}^{-2}$)	d (nm)
850	10.12	33.38	0.9294	1.691	1.316	0.036	45.34	1.27 ± 0.09
Error%	0.7577	0.6147	0.1447	9.144				
900	7.7	29.31	0.9458	1.716	1.389	0.037	36.69	1.57 ± 0.11
Error%	0.7987	0.6285	0.1399	8.044				
950	9.187	24.86	0.9512	1.973	0.715	0.027	30.36	1.90 ± 0.07
Error%	0.5676	0.4505	0.1002	5.553				
1000	11.79	22.87	0.9502	2.181	0.725	0.027	28.07	2.05 ± 0.05
Error%	0.5774	0.4562	0.1041	6.011				

Table 4

Equivalent circuit parameters for annealed Ti80 alloys after 2.5 h immersion in 5 M HCl solution: R_s solution resistance, CPE_{dl} and CPE_f constant phase elements, n_{dl} and n_f are the exponent of CPE_{dl} and CPE_f , respectively, R_{ct} charge transfer resistance, R_f resistance of the corrosion product. The Chi-square parameter (χ^2) and sums of squares (λ^2) obtained for each annealed Ti80 alloy. Moreover, the calculated electrical double layer capacitance C_{dl} and corrosion product film capacitance C_f are listed.

Annealing Temperature (°C)	R_s ($\Omega \text{ cm}^2$)	CPE_{dl} ($10^{-5} \text{ S}\cdot\text{s}^n \text{ cm}^{-2}$)	n_{dl}	R_{ct} ($\Omega \text{ cm}^2$)	CPE_f ($10^{-3} \text{ S}\cdot\text{s}^n \text{ cm}^{-2}$)	n_f	R_f ($\Omega \text{ cm}^2$)	χ^2 (10^{-3})	λ^2	C_{dl} ($10^{-5} \text{ F cm}^{-2}$)	C_f ($10^{-3} \text{ F cm}^{-2}$)
850	6.978	35.21	0.933	291.8	76.99	1	158.1	0.277	0.017	22.83	76.99
Error%	0.2951	1.017	0.2219	0.5178	8.462	3.485	7.152				
900	7.138	50.06	0.9422	305	66.18	1	170	0.204	0.014	35.38	66.18
Error%	0.2436	0.8191	0.1924	0.498	7.124	2.907	5.659				
950	6.203	47.71	0.9414	320.5	62.9	0.9989	188.3	0.285	0.017	33.16	63.07
Error%	0.2917	0.9404	0.216	0.579	8.196	3.351	6.738				
1000	10.43	25.86	0.9355	429.8	79.77	1	220.7	0.103	0.01	17.17	79.77
Error%	0.1781	0.6062	0.1347	0.3081	6.865	2.755	7.078				

All fitting errors are below 10 %, thereby representing a good fit [45].

Generally, polarization resistance (R_p) can be used to evaluate the corrosion resistance, a higher R_p indicating improved resistance [46]. In this study, R_p can be calculated using the following relationships [46,47]: $R_p = R_f$ for the circuit in Fig. 8a, but $R_p = R_f + R_{ct}$ for the circuit in Fig. 8b. According to Table 3, in 3.5 wt.% NaCl solu-

tion, R_p increases from $1.691 \times 10^6 \Omega \cdot \text{cm}^2$ to $2.181 \times 10^6 \Omega \cdot \text{cm}^2$ when the annealing temperature increases from 850 to 1000 °C. This can be attributed to the thickened oxide film. The thickness of an oxide film, d , can be obtained using the following formula [48]:

$$d = \varepsilon \varepsilon_0 / C \quad (14)$$

where ε is the relative dielectric constant of oxide film, ε_0 is the permittivity of free space (8.8542×10^{-14} F. cm $^{-1}$), and C is the capacitance of oxide film. Based on previous studies [49], the oxide film formed on titanium has a characteristic like rutile; therefore, a value of 65 is assumed for ε in this study, corresponding to the dielectric constant of rutile TiO $_2$ [49,50]. The capacitance C can be calculated using Eq. (4) [48,51,52]:

$$C = (QR^{1-n})^{1/n} \quad (15)$$

where Q is the magnitude of CPE, n is the CPE exponent, and R is a resistor in parallel with the corresponding CPE. The calculated oxide film capacitance C and thickness d of annealed Ti80 alloys in 3.5 wt.% NaCl solution are also listed in Table 3. Clearly, the oxide film thickness d monotonically increases with annealing temperature, corresponding to the enhanced polarization resistance R_p . For 5 M HCl solution, Table 4 illustrates that both charge transfer resistance R_{ct} and corrosion product film resistance R_f increase with the increase in annealing temperature, revealing an enhancement of corrosion resistance. The electrical double layer capacitance (C_{dl}) can be derived from CPE using Brug's formula [48,53]:

$$C_{dl} = CPE^{1/n} (R_s^{-1} + R_{ct}^{-1})^{(n-1)/n} \quad (16)$$

The calculated values of C_{dl} and C_f are also presented in Table 4. The value of C_{dl} is at the level of 10^{-5} F. cm $^{-2}$, which is a typical electrical double layer capacitance value [54,55]. A high value of C_f , on the order of 10^{-3} F. cm $^{-2}$, can be attributed to the appearance of corrosion product film [23,56,57]. Variations in R_p vs. annealing temperature in 3.5 wt.% NaCl and 5 M HCl solutions are plotted in Fig. 8c, d, respectively. Clearly, R_p increases with the increase in annealing temperature in both tested solutions. This phenomenon again confirms that the corrosion resistance enhances with the increase in annealing temperature.

3.2.4. Static immersion testing

Static immersion tests were carried out in 5 M HCl solution to discern further details of the corrosion processes in annealed Ti80 alloys. Fig. 9a displays variations in cumulative weight loss with immersion time. As annealing temperature increases from 850 to 1000 °C, the weight loss decreases from 19.08 mg/cm 2 to 13.06 mg/cm 2 after 10 days of immersion, demonstrating that the corrosion resistance of Ti80 alloy can be improved by adjusting annealing temperature. In addition, variations in weight loss over time present a linear increase, revealing that the corrosion rate is constant. In this study, the corrosion rate I can also be calculated using Eq. (17) [58]:

$$I = KW/AT\rho \quad (17)$$

where K is a constant (8.76×10^4), W is the weight loss in g, A is the exposed area of specimen in cm 2 , T is the exposure time in hours, and ρ is the density in g/cm 3 . Variations in the corrosion rate I with annealing temperature is plotted in Fig. 9b. The alloy annealed at 1000 °C exhibits the lowest corrosion rate, which can be attributed to highest volume fraction of β phase and thinnest α phase. The corrosion rates calculated from weight loss are also shown in Table 2 for comparison. In 5 M HCl solution, the corrosion rates (mm. year $^{-1}$) obtained from corrosion current density and weight loss are in a good agreement.

Fig. 9c-f depicts the corrosion surface morphologies of annealed Ti80 alloys. All alloys display evidence of homogeneous corrosion. No corrosion pitting is observed on surface, indicative of the excellent pitting resistance of all annealed alloys in 5 M HCl solution. Moreover, SEM observation reveals that the regions of preferential dissolution are concentrated on prior- β grain boundaries and α phases. The severe intergranular corrosion presented in Fig. 9d-f could be attributed to the segregation of impurities to these grain

boundaries [13]. As annealing temperature increases (Fig. 9d-f), the severity of intergranular corrosion is alleviated, most probably due to the reduced degree of segregation. Fig. 9g-j shows the representative back-scattered electron (BSE) images of annealed Ti80 alloys in cross-section after 10 days of immersion in 5 M HCl solution. The average values of maximum local corrosion depth marked in Fig. 9g-j are obtained from at least ten cross-section images to eliminate statistical error. The maximum local corrosion depth decreases from 20.1 ± 1.2 μ m to 10.8 ± 1.3 μ m with increasing annealing temperature from 850 to 1000 °C, revealing that the corrosion degree can be alleviated by increasing annealing temperature.

3.2.5. X-ray photoelectron spectroscopy (XPS) analysis

XPS spectra were obtained to analyze the composition of corrosion product films of annealed Ti80 alloys. Fig. 10a displays a typical XPS wide-survey spectra, indicating the presence of Ti 2p, Al 2p, Nb 3d, Zr 3d, Mo 3d, O 1s, C 1s, and N 1s. The existence of C 1s and N 1s can be ascribed to the surface contamination of specimens during the tests [11]. Fig. 10b exhibits the high-resolution spectra of Ti 2p; the peak at ~ 464.2 eV can be fitted as a doublet, corresponding to TiO $_2$ at ~ 464.5 eV and Ti $_2$ O $_3$ at ~ 462.8 eV. The peak at ~ 458.6 eV can also be fitted as a doublet, typical of TiO $_2$ at ~ 458.5 eV and Ti $_2$ O $_3$ at ~ 457.4 eV. In addition, metallic Ti, which appears at ~ 453.9 eV (Ti 2p $_{3/2}$), is also detected for all annealed alloys. This is probably a result from the substrate, indicating that a thin corrosion product film forms on surface [22,30]. The shapes of O 1s peaks of annealed alloys are similar, as seen in Fig. 10c. The O 1s spectra can be fitted to three distinctive components: O $^{2-}$ (~ 530 eV), OH $^{-}$ (~ 531 eV), and O $^{2-}$ (H $_2$ O) (~ 532 eV) [59,60]; this indicates that the corrosion product films comprise a mixture of oxides and hydroxides.

The Nb 3d spectra presented in Fig. 10d exhibit two main peaks at ~ 210.0 eV and ~ 207.4 eV. These two peaks can be assigned to the presence of Nb $_2$ O $_5$ in the corrosion product films [61]. Moreover, a small peak is observed at ~ 202.3 eV, corresponding to metallic Nb (3d $_{5/2}$), which also emanates from the substrate. For the Zr 3d spectra (Fig. 10e), two main peaks are clearly observed at ~ 182.0 eV and ~ 184.1 eV, typical of ZrO $_2$ peaks [62]. In Fig. 10f, the Mo 3d spectra show one main peak at ~ 229.4 eV, which can be attributed to the presence of MoO $_2$ [30]. As mapped in Fig. 10g, the peak in Al 2p spectra at ~ 74.6 eV can be ascribed to the presence of Al $_2$ O $_3$ [8], but the peak is weak, indicating that the corrosion product films only contain a small amount of Al $_2$ O $_3$.

4. Discussion

4.1. Corrosion mechanisms

According to previous reports [27,63–66], native oxide films for annealed Ti80 alloys are primarily composed of TiO $_2$, Al $_2$ O $_3$, Nb $_2$ O $_5$ and ZrO $_2$, which are considered to be thermodynamically stable in presence of oxygen, and of MoO $_2$:



The presence of MoO $_2$ instead of MoO $_3$ in native oxide films is based on the study reported by Park et al. [66]. Specifically, the major molybdenum species in native oxide films of Ti-Mo alloys containing a small amount of molybdenum is generally Mo $^{4+}$. In this study, as studied alloys contain only 1 wt.% molybdenum, it

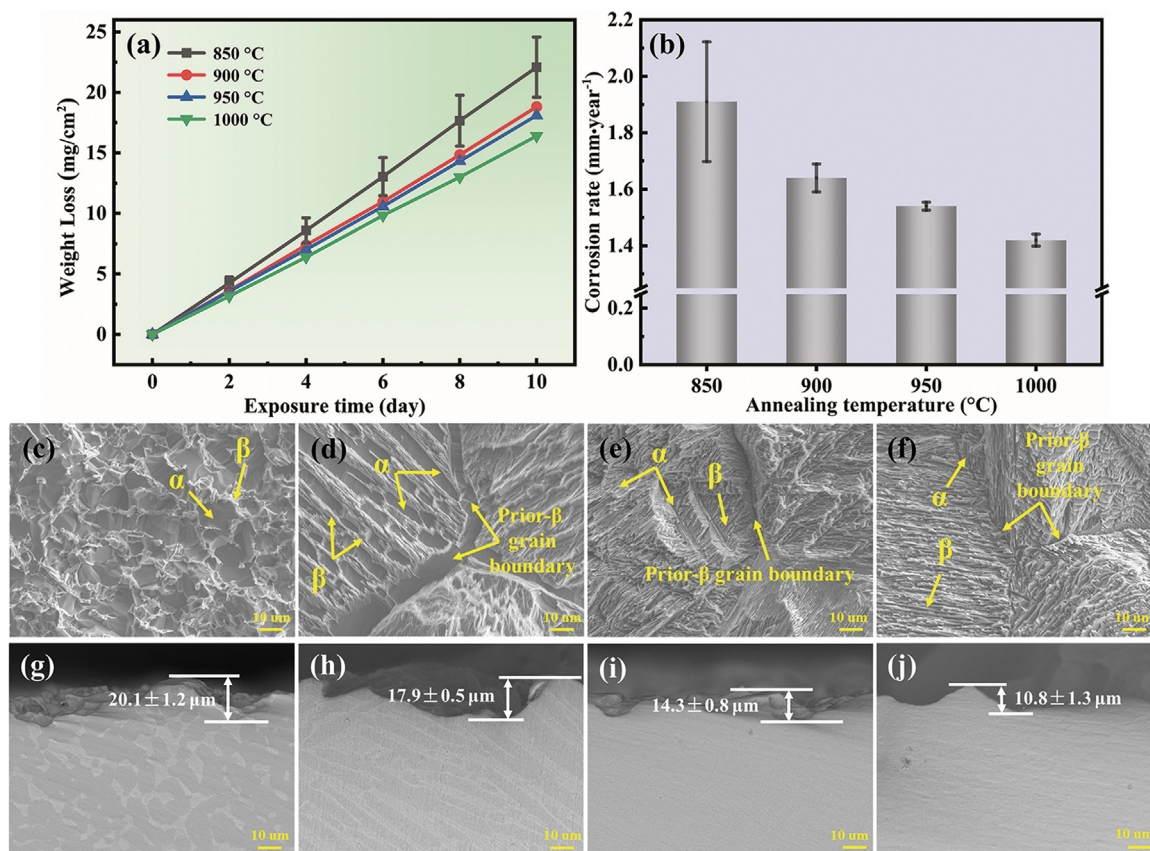


Fig. 9. Results of static immersion tests. (a) Variations in loss of mass with time for annealed Ti80 alloys in 5 M HCl solution for 10 days. (b) Corrosion rate varies with annealing temperature. (c–f) SEM images of the morphologies of corroded surface, and (g–j) cross section BSE images of annealed Ti80 alloys in 5 M HCl solution after 10 days immersion, at (c) and (g) 850 °C, (d) and (h) 900 °C, (e) and (i) 950 °C, (f) and (j) 1000 °C.

can be concluded that molybdenum oxide is present in native oxide films in the form of MoO₂.

In 3.5 wt.% NaCl solution, the terminal value of OCP (Fig. 4a) in each annealed Ti80 alloy corresponds to the thermodynamically stable range of TiO₂, Al₂O₃, ZrO₂, Nb₂O₅, and MoO₂, as demonstrated by the overlays of OCP with the standard 25 °C E–pH diagrams of Ti, Al, Nb, Zr, and Mo, respectively [67]. This indicates that native oxide films can be stably present in 3.5 wt.% NaCl solution from a thermodynamic perspective. The OCP curves (Fig. 4a) also show that no obvious dissolution of native oxide films occurs in 3.5 wt.% NaCl solution, *i.e.*, no sharp drop in potential is observed. Additionally, EIS results (Figs. 7a, 7b, and 8 a) indicate the formation of a highly compact and stable film on those annealed Ti80 alloys in 3.5 wt.% NaCl solution. Accordingly, annealed Ti80 alloys present a low current density (10⁻⁶ A/cm²) in Fig. 6a and high polarization impedance (10⁶ Ω·cm²) in Table 3.

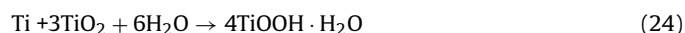
However, in 5 M HCl solution, Ti³⁺, Al³⁺, Zr⁴⁺, NbO₂ and Mo are all thermodynamically stable for each annealed Ti80 alloy at their respective OCP according to the standard 25 °C E–pH diagrams for Ti, Al, Nb, Zr and Mo [67]. This suggests that native oxide films will be dissolved when annealed Ti80 alloys are immersed in 5 M HCl solution. In fact, each OCP curve (Fig. 4b) exhibits a clear active dissolution behavior in 5 M HCl solution, corresponding to the dissolution of native oxide films. Fig. 4b reveals that the breakdown of native oxide films can be achieved after one hour immersion. As displayed in Fig. 11, we give two schematic diagrams to illustrate the salient corrosion mechanisms for annealed Ti80 alloys in 5 M HCl solution, where the chemical corrosion process has two steps, namely, the dissolution of native oxide films and dissolution of substrate. Although native ZrO₂, Nb₂O₅ and MoO₂ oxides are

thermodynamically unstable according to the standard 25 °C E–pH diagrams, they are kinetically resistant to the chemical dissolution in 5 M HCl [19]. The Nb 3d (Fig. 10d), Zr 3d (Fig. 10e) and Mo 3d spectra (Fig. 10f) reveal the presence of Nb₂O₅, ZrO₂ and MoO₂ in oxide films in 5 M HCl solution, proving the rationality of kinetic stability of those oxides. Hence, the breakdown of native oxide films mainly corresponds to the chemical dissolution of Al₂O₃ and TiO₂, as presented in Fig. 11a. When specimens are immersed in 5 M HCl solution, Al₂O₃ will firstly react with HCl, as described by the following reaction:



A weak Al₂O₃ peak presented in the Al 2p spectra (Fig. 10g) indicates that only a small amount of Al₂O₃ existed in corrosion product films in 5 M HCl solution. This can be attributed to the dissolution of Al₂O₃ through reaction (23).

In addition, the chemical dissolution of native oxide films should be mainly attributed to the conversion of TiO₂ to aqueous Ti³⁺, which generally requires two steps (Fig. 11a). First, TiO₂ is reduced to TiOOH, or its hydrated form of TiOOH·H₂O. The TiO₂ reduction reaction is balanced by oxidizing substrate. Hence, the overall process can be presented using the following reaction [19,68,69]:



Second, TiOOH·H₂O is rapidly dissolved to Ti³⁺ through the following reaction [8]:



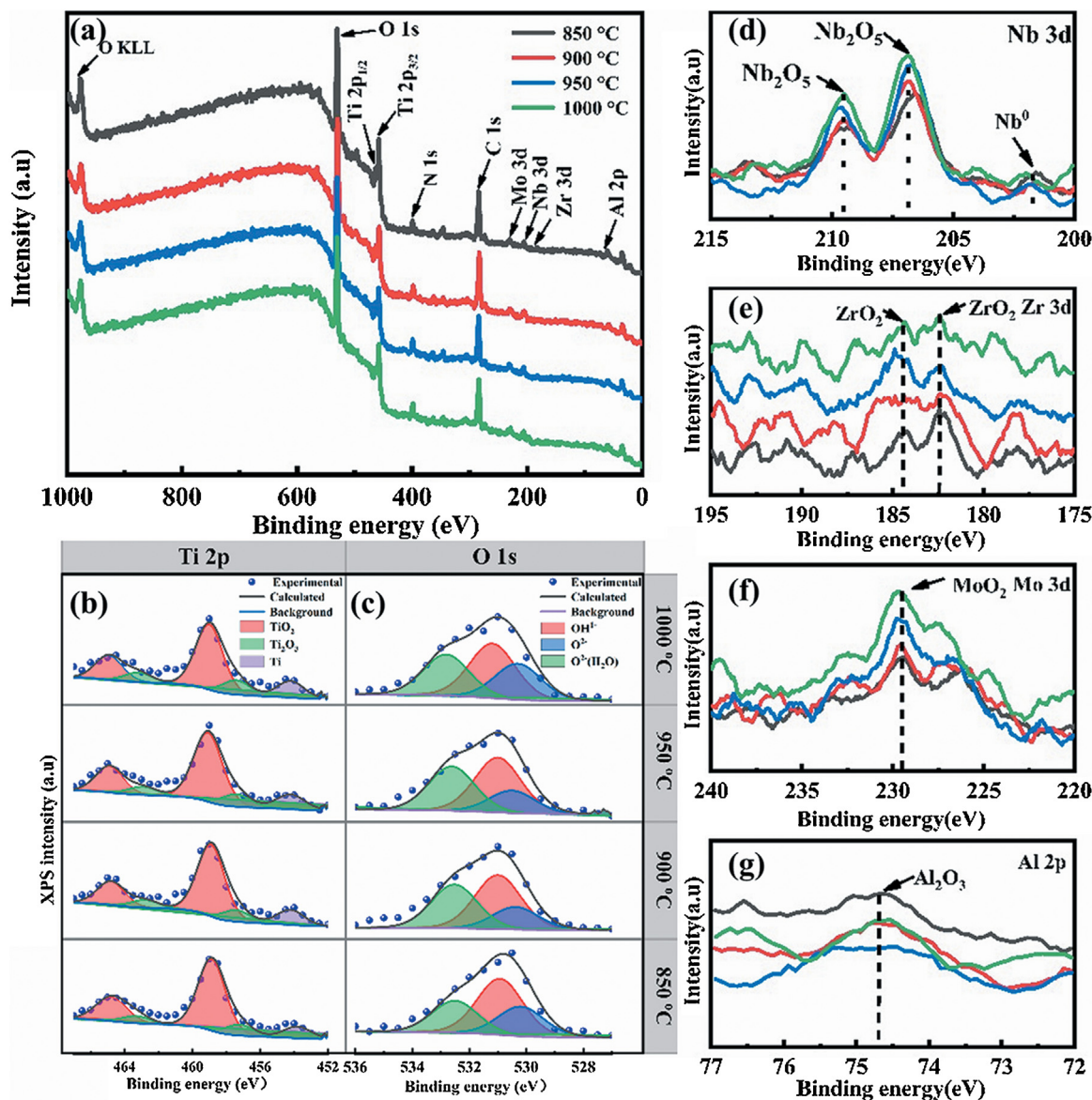


Fig. 10. Results of XPS measurements for annealed Ti80 alloys. (a) Typical survey spectra from XPS; detailed spectra from (b) Ti 2p, (c) O 1s, (d) Nb 3d, (e) Zr 3d, (f) Mo 3d and (g) Al 2p, all measured from the surface of annealed Ti80 alloys after 10 days of immersion in 5 M HCl solution.

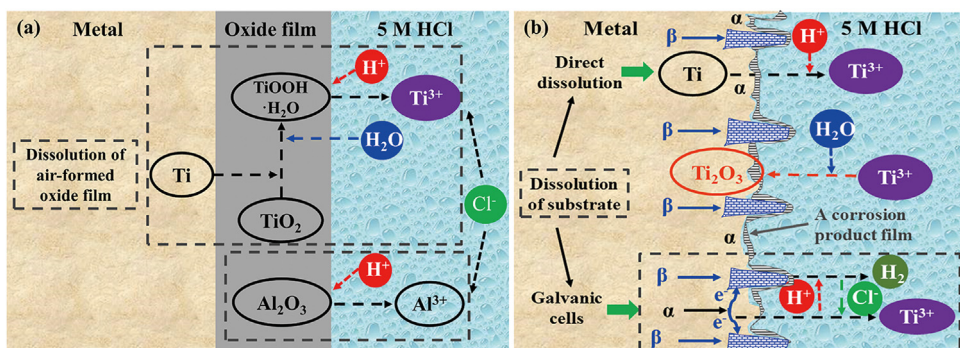


Fig. 11. Schematic diagrams of salient corrosion mechanisms in annealed Ti80 alloys in 5 M HCl solution, showing (a) dissolution of native oxide film, and (b) dissolution of substrate.

The high H^+ concentration in 5 M HCl solution makes Ti^{3+} more stable than $TiOOH \cdot H_2O$ by promoting the progress of reaction (25), a main precursor for the breakdown of native oxide films.

The breakdown of native oxide films needs only about an hour based on OCP curves (Fig. 4b). Although EIS measurements (Figs. 7b, d, and 8b) reveal the presence of a corrosion product film on surface

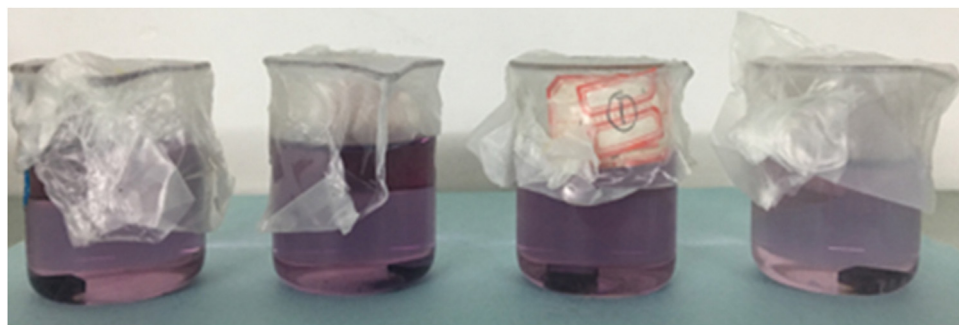


Fig. 12. The solutions of annealing Ti80 alloys after 10 days of immersion in 5 M HCl.

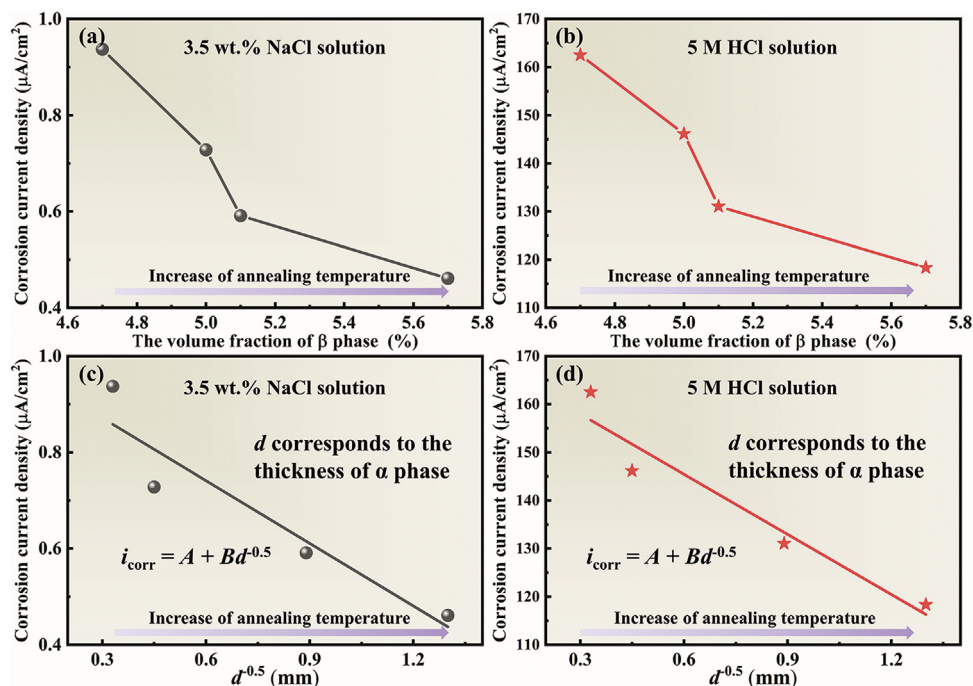


Fig. 13. The relationship between the corrosion current density and volume fraction of β phase in (a) 3.5 wt.% NaCl and (b) 5 M HCl; corresponding relationship between the corrosion current density and thickness of α phase in (c) 3.5 wt.% NaCl and (d) 5 M HCl.

of annealed Ti80 alloys in 5 M HCl solution, this corrosion product film is generally a porous and nonprotective film, as demonstrated by Cui et al. [23]. Hence, it is inevitable that the substrate Ti will be oxidized to form soluble Ti^{3+} ions (Fig. 11b) based on the chemical reactions (1) - (6) [26,70], consistent with the active dissolution behavior of anodic polarization curves (Fig. 5b). The conversion of Ti to Ti^{3+} is one of main causes for the corrosion of annealed Ti80 alloys.

As depicted in Fig. 12, the solutions remaining after 10 days of immersion exhibit a purple color, corresponding to the color of TiCl_3 , indirectly indicating the presence of Ti^{3+} . After a period of time, the accumulated Ti^{3+} ions and correspondingly reduced pH of solution may promote the formation of Ti_2O_3 through the following reaction [71]:



The Ti 2p spectra (Fig. 10b) indicate the presence of Ti_2O_3 in corrosion product films formed in 5 M HCl solution, proving the rationality of reaction (26). Apart from the chemical dissolution, the formation of micro-galvanic couple effects between α and β phases, i.e., electrochemical corrosion, is another cause for the corrosion of alloys, as illustrated in Fig. 11b. These effects stem from

the segregation of elements, as seen in Table 1; the α phase act as an anode during micro-galvanic corrosion together with β phase, which will promote the preferential dissolution of α phase.

4.2. Effect of β -Phase volume fraction and α -Phase thickness on corrosion behavior

As reported previously [[73,74],13,18,72], volume fraction of β phase plays an important role in affecting the corrosion performance of Ti alloys. Fig. 13a, b respectively shows the relationship between corrosion current density and volume fraction of β phase in 3.5 wt.% NaCl and 5 M HCl solutions. The corrosion current density decreases with the increase in volume fraction of β phase in both tested solutions, i.e., the corrosion resistance enhances with increasing volume fraction of β phase. This can be attributed to the fact that β phase is more resistant to chemical corrosion than α phase. AFM measurements were performed to prove this. Fig. 14a-d displays the 3D AFM images of corroded surface of annealed Ti80 alloys after 4 h of immersion in 5 M HCl solution. Combined with the analysis of SEM and HADDF images in Fig. 3e-h, j, the distribution of α and β phases on corroded surface of annealed Ti80 alloys can be identified, also as presented in Fig. 14a-d. From the

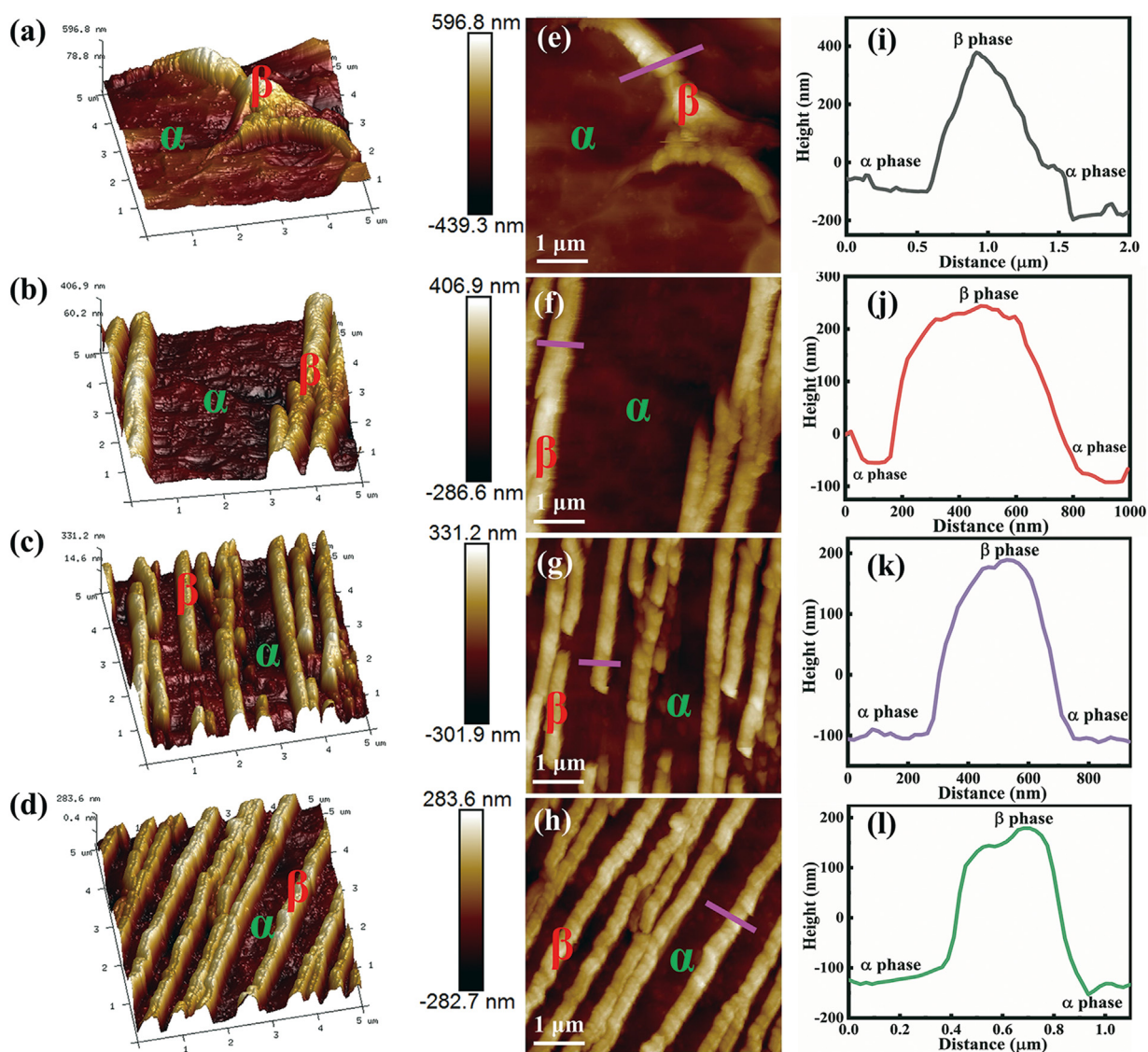


Fig. 14. 3D and 2D AFM images of annealed Ti80 alloys after 4 h immersion in 5 M HCl solution, at (a) and (e) 850 °C, (b) and (f) 900 °C, (c) and (g) 950 °C, (d) and (h) 1000 °C. Line-profile analysis of relative height of β phase, at (i) 850 °C, (j) 900 °C, (k) 950 °C and (l) 1000 °C.

latter figures, it is evident that α phase acts as a location for preferential dissolution. With respect to their separation, the evolution of height with distance between adjacent α and β phases can be evaluated using line-profile analysis, as shown in the pink lines in Fig. 14e-h. AFM data showing how the height varies across these pink lines due to such selective phase dissolution are plotted in Fig. 14i-l. The height of α phase is lower than that of β phase for all annealed Ti80 alloys, indicating that α phase is the more susceptible of phases to corrosion. Indeed, the preferential corrosion of α phase can be attributed to element segregation. In Fig. 3j and Table 1, Al element is fertile in α phase, while Nb, Zr, and Mo tend to be distributed in β phase. Consequently, we could deduce that the native oxide films of β phase are mainly composed of Nb_2O_5 , MoO_2 and ZrO_2 , as compared to more Al_2O_3 appeared on the surface of α phase. As mentioned in section 4.1, Al_2O_3 will be dissolved firstly through reaction (23) since Nb_2O_5 , MoO_2 and ZrO_2 have a higher stability than Al_2O_3 [73,74]. Besides, we can also presume that more TiO_2 exists in the native oxide films of α phase due to its higher Ti content, as shown in Table 1. The preferential dissolution of Al_2O_3 and conversion from TiO_2 to aqueous Ti^{3+} through reactions (24) - (25) should be responsible for the breakdown of

these native oxide films. Therefore, it is reasonable to infer that α phase preferentially loses the protection of native oxide films to be less resistant to corrosion. Subsequently, without the protection of native oxide films, substrate α phase suffers severer active chemical corrosion (the dissolution from Ti to Ti^{3+}) than β phase through chemical reactions (1) - (6), which is also ascribed to its higher Ti content.

In addition, the thickness of α phase can also significantly affect the corrosion resistance of annealed Ti80 alloys. Ralston et al. [75] established a relationship between corrosion rate and grain size based on their own results and prior studies in the literature. They proposed the relationship between corrosion current density and grain size as:

$$i_{\text{corr}} = A + Bd^{-0.5} \quad (27)$$

where A is a function of environment, B is a material constant related to composition or impurity level, and d is the grain size. Yang et al. also reported a similar relationship between the thickness of α phase d and corrosion current density i_{corr} [13]. To evaluate the effect of thickness of α phase on the corrosion performance of annealed Ti80 alloys, variations of α -phase thickness d with the

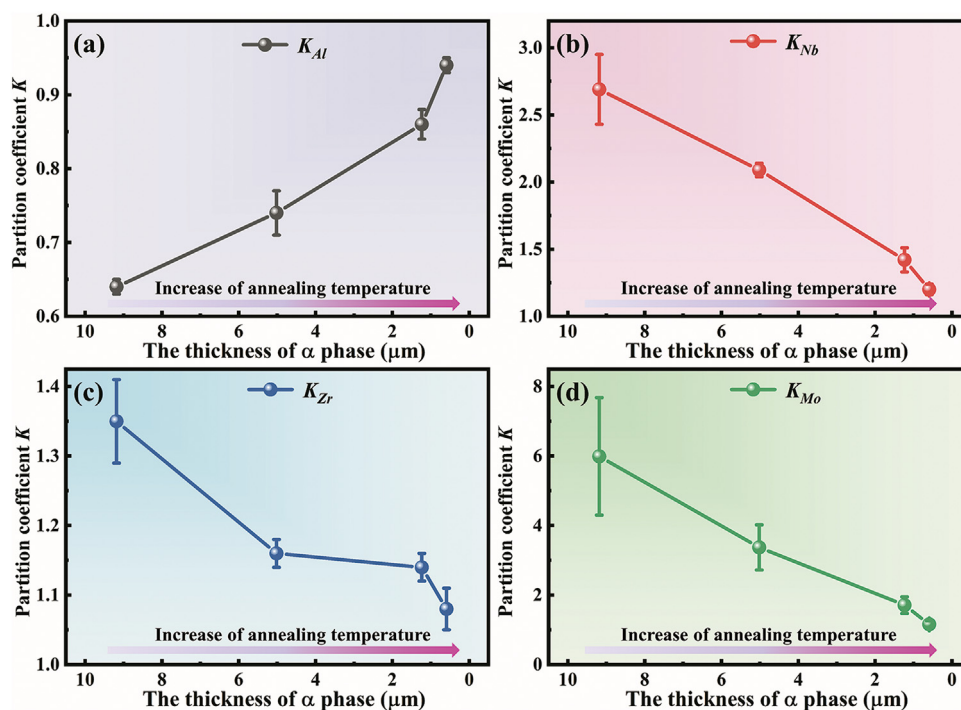


Fig. 15. Variations in the partition coefficient of alloying elements with the thickness of α phase, in (a) Al, (b) Nb, (c) Zr, and (d) Mo.

corrosion current density i_{corr} are plotted in Fig. 13c, d, respectively for 3.5 wt.% NaCl and 5 M HCl solutions. Relatively good linear relationships with negative slopes can be seen for both solutions. These results indicate that as the thickness of α phase d decreases, the corrosion resistance of annealed Ti80 alloys increases, which we believe is associated with two factors. Firstly, the aggregation of elements in α or β phase can clearly be reduced by refining its thickness. To evaluate the degree of segregation of alloying elements in α and β phases, a single partition coefficient K_i for element i can be defined as follows [76]:

$$K_i = C_i^\beta / C_i^\alpha \quad (28)$$

where C_i^β and C_i^α are, respectively, the concentration of element i in adjacent β and α phases. As the value of K_i tends to unity, the lighter the degree of segregation. Fig. 15 presents variations in partition coefficient K with the thickness of α phase d . As the α -phase thickness reduces, the value of K_{Al} (Fig. 15a) increases to approach 1, while the values of K_{Nb} (Fig. 15b), K_{Zr} (Fig. 15c) and K_{Mo} (Fig. 15d) all decrease to approach 1, indicating that the degree of segregation of elements Al, Nb, Zr and Mo can all be alleviated with a reduced thickness of α phase. As illustrated in Fig. 11b, the emergence of harmful micro-galvanic couple effects between α and β phases should be one of the main causes for the corrosion of annealed Ti80 alloys; these galvanic cells originate from the different electrochemical activities of α and β phases, which corresponds to the uneven distribution of alloying elements in these phases. (Table 1). The degree of this segregation can be alleviated by increasing annealing temperature due to a reduced thickness of α phase, as indicated by Fig. 15, which serves to diminish micro-galvanic couple effects. Secondly, the small α phase and high fraction of phase boundaries can promote the formation of oxide films [13,75]. Because the formation of oxide films is a diffusion-controlled process, phase boundaries play a considerable role in providing short diffusion channels for ions. Such preferential diffusion of Ti, Al, Nb, Zr, Mo and O can occur at phase boundaries to provide more oxidation and active sites for the formation of oxide films.

In short, the enhanced corrosion resistance of annealed Ti-6Al-3Nb-2Zr-1Mo (Ti80) alloys, which can be attained by increasing annealing temperature from 850 to 1000 °C, can be principally attributed to the combined effects of an increased volume fraction of β phase with the reduced thickness of α phase.

5. Conclusions

The microstructure and corrosion behavior of annealed Ti80 alloys in NaCl and HCl solutions have been evaluated. The main conclusions of this study are as follows:

- (1) Microstructural characterization shows that Ti80 alloy annealed at a higher temperature generates a higher fraction of β phase and more refined lamellar α phase.
- (2) Based on results of potentiodynamic polarization curves, all annealed Ti80 alloys are seen to exhibit spontaneous passivation behavior in 3.5 wt.% NaCl solution and active to passive behavior in 5 M HCl solution. Accompanying electrochemical impedance spectroscopy results reveal that one compact oxide film is formed in 3.5 wt.% NaCl solution, and a corrosion product film is present in 5 M HCl solution.
- (3) Both electrochemical and static immersion tests indicate that the corrosion resistance of annealed Ti80 alloys increases with increasing annealing temperature, which can be attributed to increased volume fraction of β phase and decreased thickness of α phase.
- (4) Atomic force microscopy observations show that β phase is more resistant to corrosion than α phase. This is related to the higher Nb, Zr, and Mo content of β phase.
- (5) The corrosion of annealed Ti80 alloys can be attributed to the micro-galvanic couple effects and chemical dissolution of native oxide film and substrate.

Acknowledgements

This research work was supported by the National Key Research and Development Program of China (2016YFB0301201), the Yunnan Rare Metal Materials Genetic Engineering Project (2018ZE013), and the National Natural Science Foundation of China (51425402 and 51671073).

References

- [1] D. Banerjee, J.C. Williams, *Acta Mater.* 61 (2013) 844–879.
- [2] B. Wu, Z. Pan, S. Li, D. Cuiuri, D. Ding, H. Li, *Corros. Sci.* 137 (2018) 176–183.
- [3] Y. Bai, X. Gai, S. Li, L.-C. Zhang, Y. Liu, Y. Hao, X. Zhang, R. Yang, Y. Gao, *Corros. Sci.* 123 (2017) 289–296.
- [4] S. Yan, G.-L. Song, Z. Li, H. Wang, D. Zheng, F. Cao, M. Horynova, M.S. Dargusch, L. Zhou, *J. Mater. Sci. Technol.* 34 (2018) 421–435.
- [5] W. Xu, X. Lu, J. Tian, C. Huang, M. Chen, Y. Yan, L. Wang, X. Qu, C. Wen, *J. Mater. Sci. Technol.* 41 (2020) 191–198.
- [6] M.A. Khan, R.L. Williams, D.F. Williams, *Biomaterials* 20 (1999) 631–637.
- [7] S. Tamilselvi, V. Raman, N. Rajendran, *Electrochim. Acta* 52 (2006) 839–846.
- [8] X. Gai, Y. Bai, J. Li, S. Li, W. Hou, Y. Hao, X. Zhang, R. Yang, R.D.K. Misra, *Corros. Sci.* 145 (2018) 80–89.
- [9] N. Dai, L.-C. Zhang, J. Zhang, X. Zhang, Q. Ni, Y. Chen, M. Wu, C. Yang, *Corros. Sci.* 111 (2016) 703–710.
- [10] N. Dai, L.-C. Zhang, J. Zhang, Q. Chen, M. Wu, *Corros. Sci.* 102 (2016) 484–489.
- [11] Y.-L. Zhou, D.-M. Luo, *J. Alloys Compd.* 509 (2011) 6267–6272.
- [12] P.A.B. Kuroda, M.L. Lourenço, D.R.N. Correa, C.R. Grandini, *J. Alloys Compd.* 815 (2020), 152108.
- [13] Y. Yang, C. Xia, Z. Feng, X. Jiang, B. Pan, X. Zhang, M. Ma, R. Liu, *Corros. Sci.* 101 (2015) 56–65.
- [14] R. Jing, S.X. Liang, C.Y. Liu, M.Z. Ma, R.P. Liu, *Mater. Des.* 52 (2013) 981–986.
- [15] M. Geetha, U. Kamachi Mudali, A.K. Gogia, R. Asokamani, B. Raj, *Corros. Sci.* 46 (2004) 877–892.
- [16] M. Atapour, A. Pilchak, G.S. Frankel, J.C. Williams, M.H. Fathi, M. Shamanian, *Corrosion*. 66 (2010), 65004-1-65004-9.
- [17] G.A. Longhitano, M.A. Arenas, A. Conde, M.A. Larosa, A.L. Jardini, C.A.D. Zavaglia, J.J. Damborenea, *J. Alloys Compd.* 765 (2018) 961–968.
- [18] C. Xia, Z. Zhang, Z. Feng, B. Pan, X. Zhang, M. Ma, R. Liu, *Corros. Sci.* 112 (2016) 687–695.
- [19] S.Y. Yu, C.W. Brodrick, M.P. Ryan, J.R. Scully, *J. Electrochem. Soc.* 146 (1999) 4429–4438.
- [20] M. Atapour, A. Pilchak, G.S. Frankel, J.C. Williams, *Corros. Sci.* 52 (2010) 3062–3069.
- [21] ASTM Standard G31–72, Standard Practice for Laboratory Immersion Corrosion Testing of Metals, ASTM Standards, West Conshohocken, 2004.
- [22] Z.B. Wang, H.X. Hu, Y.G. Zheng, W. Ke, Y.X. Qiao, *Corros. Sci.* 103 (2016) 50–65.
- [23] Z. Cui, L. Wang, M. Zhong, F. Ge, H. Gao, C. Man, C. Liu, X. Wang, *J. Electrochem. Soc.* 165 (2018) C542–C561.
- [24] G.R. Argade, S.K. Panigrahi, R.S. Mishra, *Corros. Sci.* 58 (2012) 145–151.
- [25] H. Liu, J. Yang, X. Zhao, Y. Sheng, W. Li, C.-L. Chang, Q. Zhang, Z. Yu, X. Wang, *Corros. Sci.* (2019), 108195.
- [26] W.B. Utomo, S.W. Donne, *Electrochim. Acta* 51 (2006) 3338–3345.
- [27] S. Ningshen, M. Sakairi, K. Suzuki, T. Okuno, *Corros. Sci.* 91 (2015) 120–128.
- [28] T.M. Chiu, M. Mahmoudi, W. Dai, A. Elwany, H. Liang, H. Castaneda, *Electrochim. Acta* 279 (2018) 143–151.
- [29] E. McCafferty, *Corros. Sci.* 47 (2005) 3202–3215.
- [30] Z.B. Wang, H.X. Hu, Y.G. Zheng, *Corros. Sci.* 130 (2018) 203–217.
- [31] M.A. Amin, S.S. Abd El Rehim, H.T.M. Abdel-Fatah, *Corros. Sci.* 51 (2009) 882–894.
- [32] D. Huang, J. Hu, G.-L. Song, X. Guo, *Electrochim. Acta* 56 (2011) 10166–10178.
- [33] G.W. Walter, *Corros. Sci.* 26 (1986) 681–703.
- [34] T.T.M. Tran, B. Tribollet, E.M.M. Sutter, *Electrochim. Acta* 216 (2016) 58–67.
- [35] A. Lasia, *Electrochemical Impedance Spectroscopy and Its Applications*, Springer, New York, 2014.
- [36] Rd.P.B. Hernández, I.V. Aoki, B. Tribollet, H.G. de Melo, *Electrochim. Acta* 56 (2011) 2801–2814.
- [37] A.K. Shukla, R. Balasubramaniam, *Corros. Sci.* 48 (2006) 1696–1720.
- [38] J. Pan, D. Thierry, C. Leygraf, *Electrochim. Acta* 41 (1996) 1143–1153.
- [39] C.L. Alexander, B. Tribollet, M.E. Orazem, *Electrochim. Acta* 173 (2015) 416–424.
- [40] C.Q. Li, D.K. Xu, X.B. Chen, B.J. Wang, R.Z. Wu, E.H. Han, N. Birbilis, *Electrochim. Acta* 260 (2018) 55–64.
- [41] L. Liu, L. Wu, X. Chen, D. Sun, Y. Chen, G. Zhang, X. Ding, F. Pan, *J. Mater. Sci. Technol.* 37 (2020) 104–113.
- [42] M.E. Orazem, B. Tribollet, *Electrochemical Impedance Spectroscopy*, John Wiley & Sons, 2011.
- [43] C. Peng, Y. Liu, H. Liu, S. Zhang, C. Bai, Y. Wan, L. Ren, K. Yang, *J. Mater. Sci. Technol.* 35 (2019) 2121–2131.
- [44] J. Yang, Y. Lu, Z. Guo, J. Gu, C. Gu, *Corros. Sci.* 130 (2018) 64–75.
- [45] K.A. Yasakau, S. Kallip, M.L. Zheludkevich, M.G.S. Ferreira, *Electrochim. Acta* 112 (2013) 236–246.
- [46] Z.B. Wang, H.X. Hu, C.B. Liu, Y.G. Zheng, *Electrochim. Acta* 135 (2014) 526–535.
- [47] A.D. King, N. Birbilis, J.R. Scully, *Electrochim. Acta* 121 (2014) 394–406.
- [48] B. Hirschorn, M.E. Orazem, B. Tribollet, V. Vivier, I. Frateur, M. Musiani, *Electrochim. Acta* 55 (2010) 6218–6227.
- [49] J. Pan, D. Thierry, C. Leygraf, *J. Biomed. Mater. Res.* 28 (1994) 113–122.
- [50] G. Bolat, J. Izquierdo, J.J. Santana, D. Mareci, R.M. Souto, *Electrochim. Acta* 88 (2013) 447–456.
- [51] M.E. Orazem, B. Tribollet, V. Vivier, D.P. Riemer, E. White, A. Bunge, *J. Braz. Chem. Soc.* 25 (2014) 532–539.
- [52] M.E. Orazem, I. Frateur, B. Tribollet, V. Vivier, S. Marcelin, N. Pèbère, A.L. Bunge, E.A. White, D.P. Riemer, M. Musiani, *J. Electrochem. Soc.* 160 (2013) C215–C225.
- [53] G.J. Brug, A.L.G. van den Eeden, M. Sluyters-Rehbach, J.H. Sluyters, *J. Electroanal. Chem.* 176 (1984) 275–295.
- [54] F. Zhang, C. Örnek, J.-O. Nilsson, *J. Pan, Corros. Sci.* (2019), 108319.
- [55] D.C. Grahame, *Chem. Rev.* 41 (1947) 441–501.
- [56] S.Y. Yu, J.R. Scully, C.M. Vitus, *J. Electrochem. Soc.* 148 (2001) B68–B78.
- [57] D.J. Blackwood, L.M. Peter, H.E. Bishop, P.R. Chalker, D.E. Williams, *Electrochim. Acta* 34 (1989) 1401–1403.
- [58] F. Yang, H. Kang, E. Guo, R. Li, Z. Chen, Y. Zeng, T. Wang, *Corros. Sci.* 139 (2018) 333–345.
- [59] H. Feng, Z. Jiang, H. Li, P. Lu, S. Zhang, H. Zhu, B. Zhang, T. Zhang, D. Xu, Z. Chen, *Corros. Sci.* 144 (2018) 288–300.
- [60] S. Ningshen, M. Sakairi, K. Suzuki, S. Ukai, *Corros. Sci.* 78 (2014) 322–334.
- [61] C.G. Jia, J. Pang, S.P. Pan, Y.J. Zhang, K.B. Kim, J.Y. Qin, W.M. Wang, *Corros. Sci.* 147 (2019) 94–107.
- [62] X. Zhang, H. Shi, B.-Q. Xu, *J. Catal.* 279 (2011) 75–87.
- [63] E. Godlewska, M. Mitoraj, K. Leszczynska, *Corros. Sci.* 78 (2014) 63–70.
- [64] J. Zheng, X. Hou, X. Wang, Y. Meng, X. Zheng, L. Zheng, *Corros. Sci.* 96 (2015) 186–195.
- [65] M. Santamaria, F. Di Quarto, H. Habazaki, *Corros. Sci.* 50 (2008) 2012–2020.
- [66] P.Y. Park, E. Akiyama, H. Habazaki, A. Kawashima, K. Asami, K. Hashimoto, *Corros. Sci.* 38 (1996) 1649–1667.
- [67] M. Pourbaix, *Atlas of Electrochemical Equilibria in Aqueous Solution*, NACE International, 1974.
- [68] C.K. Dyer, *J. Electrochem. Soc.* 125 (1978) 23–29.
- [69] D.J. Blackwood, L.M. Peter, D.E. Williams, *Electrochim. Acta* 33 (1988) 1143–1149.
- [70] C.K. Dyer, J.S.L. Leach, *Electrochim. Acta* 23 (1978) 1387–1394.
- [71] T. Furuya, J. Kawafuku, H. Satoh, K. Shimogori, A. Aoshima, S. Takeda, *Isij Int.* 31 (1991) 189–193.
- [72] J.-R. Chen, W.-T. Tsai, *Electrochim. Acta* 56 (2011) 1746–1751.
- [73] W.Y. Guo, J. Sun, J.S. Wu, *Mater. Chem. Phys.* 113 (2009) 816–820.
- [74] M.A. Khan, R.L. Williams, D.F. Williams, *Biomaterials* 20 (1999) 631–637.
- [75] K.D. Ralston, N. Birbilis, C.H.J. Davies, *Scr. Mater.* 63 (2010) 1201–1204.
- [76] J. Wan, Y. Lou, H. Ruan, *Corros. Sci.* 139 (2018) 13–20.